Posted on 8 Feb 2023 — The copyright holder is the author/funder. All rights reserved. No reuse without permission. — https://doi.org/10.22541/au.167584896.64632955/v1 — This a preprint and has not been peer reviewed. Data may be preliminary.

Compositionally modulated FeMn bimetallic skeletons for highly efficient overall water splitting

Licheng Huang[1], Ruiqi Yao[2], Zili Li[3], Jiaxin He[1], Yingqi Li[2], Hongxiang Zong[4], Shuang Han[1], Jianshe Lian[1], Yangguang Li[2], and Xiangdong Ding[4]

[1]Jilin University
[2]Northeast Normal University
[3]Changchun Institute of Biological Products Co Ltd
[4]Xi'an Jiaotong University

February 8, 2023

Abstract

Transition metal-based nanomaterials exhibit promising potential as highly active and low-cost electrocatalyst for alkaline water splitting, which can be achieved via elaborating compositional modulation and structural manipulation. This, however, normally involves multiple or even complex synthetic procedures. Herein, we report a simple one-step sulfidation of FeMnZn multi–metal skeletons for the preparation of highly efficient electrocatalysts. The incorporation of Mn and Zn induced hierarchical nano/micro sheet–to–sheet supported on open porous skeleton (FeMnZn/Mn-FeS, FMZS2), which not only facilitates electron/ion transport but also expands the accessible surface. Meanwhile, the Mn is introduced to optimize the adsorption/desorption ability of intermediates on the S sites in FeS. The resultant effect leads to remarkable electrocatalytic performance with good durability. Notably, the optimized FMZS2 delivers a 20 mA cm–2 at low overpotential of 118 mV for HER and a 100 mA cm–2 at overpotential of 390 mV for OER, outperfoming Pt/C and IrO2 catalyst, respectively. Moreover, the assembled alkaline electrolyzer also has good overall water splitting capability, which is better than that of the noble metal ones.

Compositionally modulated FeMn bimetallic skeletons for highly efficient overall water splitting

Licheng Huang, Ruiqi Yao, Zili Li, Jiaxin He, Yingqi Li*, Hongxiang Zong*, Shuang Han*, Jianshe Lian, Yangguang Li, Xiangdong Ding

Dr. L. C. Huang, Dr. J. He, Prof. S. Han, Prof. J. S. Lian

Key Laboratory of Automobile Materials, Ministry of Education, School of Materials Science and Engineering

Jilin University

Changchun 130022, China

E-mail: shuanghan@jlu.edu.cn

Dr. R. Yao, Dr. Y. Q. Li, Prof. Y. Li

Key Laboratory of Polyoxometalate and Reticular Material Chemistry of Ministry of Education, Faculty of Chemistry

Northeast Normal University

Changchun 130024, China

E-mail: liyq164@nenu.edu.cn

Prof. H. Zong, Prof. X. Ding

State Key Laboratory for Mechanical Behavior of Materials

Xi'an Jiaotong University

Xi'an 710049, China

Ms. Z. Li

Vaccine Room 1

Changchun Institute of Biological Products Co Ltd

Changchun 130022, PR China

Abstract

Transition metal-based nanomaterials exhibit promising potential as highly active and low-cost electrocatalyst for alkaline water splitting, which can be achieved via elaborating compositional modulation and structural manipulation. This, however, normally involves multiple or even complex synthetic procedures. Herein, we report a simple one-step sulfidation of FeMnZn multi–metal skeletons for the preparation of highly efficient electrocatalysts. The incorporation of Mn and Zn induced hierarchical nano/micro sheet–to–sheet supported on open porous skeleton (FeMnZn/Mn-FeS, FMZS2), which not only facilitates electron/ion transport but also expands the accessible surface. Meanwhile, the Mn is introduced to optimize the adsorption/desorption ability of intermediates on the S sites in FeS. The resultant effect leads to remarkable electrocatalytic performance with good durability. Notably, the optimized FMZS2 delivers a 20 mA cm^{-2} at low overpotential of 118 mV for HER and a 100 mA cm^{-2}at overpotential of 390 mV for OER, outperfoming Pt/C and IrO_2 catalyst, respectively. Moreover, the assembled alkaline electrolyzer also has good overall water splitting capability, which is better than that of the noble metal ones.

1. Introduction

Consumption of traditional fossil fuels and the accompanying environmental concerns, *e.g.* emission of greenhouse gases (CO_2, N_2O, etc.), stimulate the ever–growing demand for renewable and clean energy.[1-5] Hydrogen is considered to be an alternative green fuel owing to its light wight and high heating value (142351 kJ kg^{-1}). Electrocatalytic water splitting is one of the promising and high–efficiency methods for hydrogen production. Nevertheless, HER and OER constitute the electrocatalytic water splitting that requires to achieve high overpotential.[6, 7] So far, the sophisticated electrocatalysts are currently recognized as noble Pt–based for HER and Ir–, Ru–based for OER.[8-11] Disappointingly, some inherent characteristics of noble metals, such as low earth abundance, exorbitant price and poor durability, hinder their practical application in large scale. To circumvent these dilemmas, focuses are placed on the development of transition metals–based materials with low–cost and high abundance, what's more, high electrocatalytic activity under operating conditions.

In recent years, the application of transition metal sulfides (TMSs) in electrocatalytic water splitting has received much attention because of its distinctive chemical and physical characteristics.[12-15]The synthesis condition of TMSs is comparatively mild in comparison to transition metal carbides or nitrides, which typically requires multi–step and high–temperature processes. Also, TMSs–based systems typically exhibit excellent conductivity compared to metal oxides owing to the relatively narrow gap between the conduction and valence bands, which makes them behave like semiconductors. More impressively, iron sulfide (FeS) has remarkable superiority compared with other counterparts due to the low cost and non–toxicity of iron.[9, 16, 17] Based on the above considerations, Fe–based sulfides electrocatalysts have been extensively investigated.[18-20] However, FeS electrocatalyst without further modifications can rarely exhibit excellent

Posted on 8 Feb 2023 — The copyright holder is the author/funder. All rights reserved. No reuse without permission. — https://doi.org/10.22541/au.167584896.64632955/v1 — This a preprint and has not been peer reviewed. Data may be preliminary.

Posted on 8 Feb 2023 — The copyright holder is the author/funder. All rights reserved. No reuse without permission. — https://doi.org/10.22541/au.167584896.64632955/v1 — This a preprint and has not been peer reviewed. Data may be preliminary.

catalytic activity for both HER and OER due to the poor intrinsic catalytic activity of the surface sites in homogeneous phase and inferior electroactive surface area in bulk structure. Doping is a judicious strategy to improve the intrinsic electrocatalytic performances by simultaneously adjusting the electronic structure of the host element to optimizing the adsorption/desorption behavior of intermediates on modified surface, as well as lowering the resistances.[15, 21-26] Furthermore, the active surface area of the electrocatalyst can be expanded by morphological engineering to maximize the number of exposed active sites. However, it is hard to develop direct synthesis technology of metal sulfides to increase their surface areas because of the volume shrinkage and electron affordability between metal and S atom.[27-29]Therefore, doping, hierarchical sheet and porous architecture are effective strategies to enhance the electrocatalytic performances.

To simultaneously fulfill these demands, we reasonably design a hierarchical integrated electrocatalyst for highly efficient water splitting through the successional etching and sulfuration process, in which electroactive Mn doped FeS (Mn–FeS) with a typical nano/micro sheet–to–sheet structures seamlessly integrated on porous FeMnZn alloy skeleton. The specially–designed FeMnZn/Mn-FeS electrocatalyst has the following characteristics: i) Mn doping trigger S sites in FeS phase with optimal adsorption and desorption of intermediate species during HER and OER to enhance the intrinsic catalytic activity; ii) hierarchical nano/micro sheet–to–sheet architecture of Mn–FeS enlarges the specific surface area, which is caused by etching Zn atoms in precursor alloy to form micro–sheet and *in situ* grown sulfide to form nano–sheet; iii) porous FeMnZn skeleton with continuous ligaments, unimpeded channels and integrated electrode structure generates efficient electron transfer and mass transport. Benefiting from all these merits, the hierarchical integrated FeMnZn/Mn-FeS electrocatalyst exhibits superb catalytic performance for water splitting. FMZS2 only requires overpotentials of 118 mV and 390 mV to achieve 20 mA cm^{-2} and 100 mA cm^{-2} for HER and OER in alkaline electrolyte, respectively, and maintains good durability. Moreover, FMZS2, served as both anode and cathode in the 1 M KOH electrolyzer, also has great overall water splitting capability, which shows an overpotential of 1.62 V at 10 mA cm^{-2}. According to the density functional theory (DFT) calculations, S sites neighbouring Mn in Mn-FeS possesses the optimal ability to adsorb/desorb intermediates during HER and OER thereby accelerating the reaction kinetics. Specically, the utilization of cost–efficient materials and facile synthesis procedure of this integrated structure enable its large–scale application for practical H_2 production from electrocatalytic water splitting.

2. Results and discussion

2.1. Morphology and structure

The synthesis process of FMZS2 consists of two steps, *i.e.* etching and sulfuration, as shown in**Figure 1a** . The porous FeMnZn skeleton (FMZ2) is prepared by etching $Fe_{70}Mn_{28}Zn_2$ (wt%, FMZ1) using 3 wt% HCl solution to selectively remove the majority of Zn and part of Mn due to the difference in metal activity, verified by the EDS spectra (**Figure S1a^{1} and b^{1}**). **Figure S1a$^{2-4}$ and b$^{2-4}$** display the scanning electron microscopy (SEM) images of FMZ1 and FMZ2 at different magnifications. The SEM images show that the surface of FMZ1 is rugged and irregular, while the surface of FMZ2 shows a large number of micro–pores and micro–sheets. XRD patterns demonstrate the major phase of FMZ2 is metallic Fe and Mn, similar with FMZ1 (**Figure S2**). Owing to open channel, micro–sheet structure and uniform phase distribution, FMZ2 is beneficial to provide permeable and conductive skeleton with abundant nucleation site for the subsequent vulcanization treatment. After sulfidation, hierarchical Mn–doped FeS nano–sheets successfully grow on the micro–sheet surfaces of FMZ2 via hydrothermal method. Both lateral and longitudinal dimension of

Posted on 8 Feb 2023 — The copyright holder is the author/funder. All rights reserved. No reuse without permission. — https://doi.org/10.22541/au.167584896.64632955/v1 — This a preprint and has not been peer reviewed. Data may be preliminary.

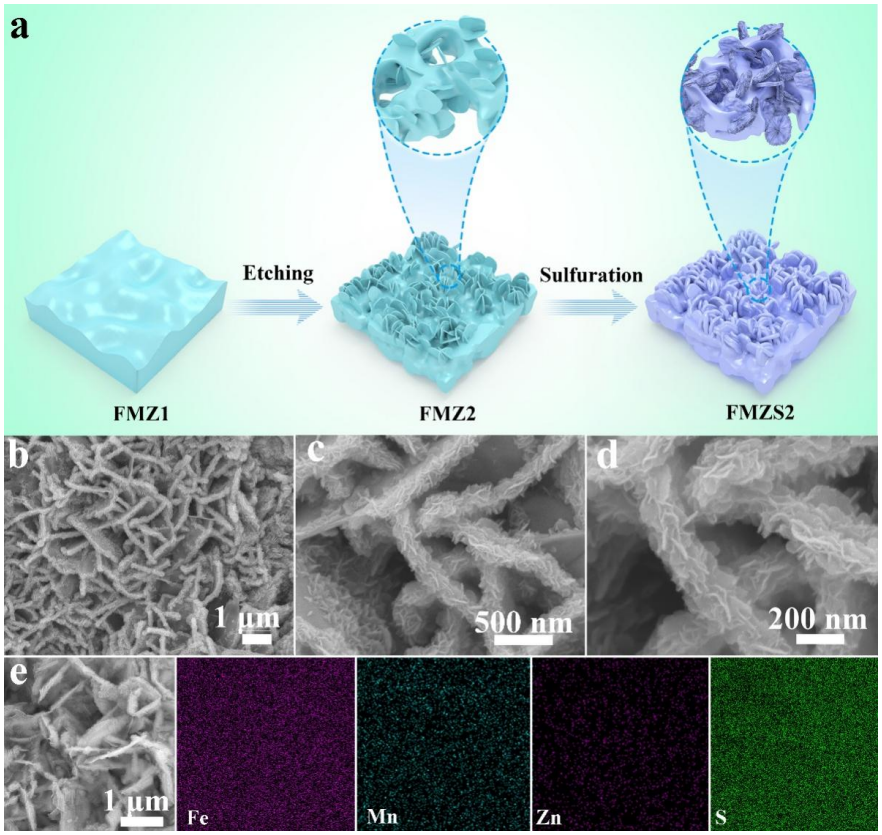

Figure 1. (a) Schematic for the synthesis of FMZS2; (b–d) SEM images and (e) EDS–mapping of FMZS2.

the micro–sheets increase and the vertical aligned nano–sheets ensure maximum effective utilization of the active surface during electrocatalytic water splitting (**Figure 1b–d**). The EDS mapping results (**Figure 1e**) show that the elements Fe, Mn, Zn and S are uniformly distributed across the FMZS2. The elemental ratio of Fe:Mn:Zn:S in FMZS2 is about 66.83 : 1.91 : 0.21 : 31.05 (wt%) according to the EDS spectra (**Figure S3a**).

The X–ray diffraction (XRD) pattern of the FMZS2 is displayed in**Figure 2a** . The characteristic peaks of FeS, metallic Fe and Mn are labeled with various shapes. The clear diffraction peaks at 30.09°, 34.50°, 38.98°, 49.59°, 50.45°, 53.02°, 59.10°, 72.75° and 85.76° correspond to (101), (110), (111), (200), (112), (201), (211), (220) and (311) crystal facets of

Posted on 8 Feb 2023 — The copyright holder is the author/funder. All rights reserved. No reuse without permission. — https://doi.org/10.22541/au.167584896.64632955/v1 — This a preprint and has not been peer reviewed. Data may be preliminary.

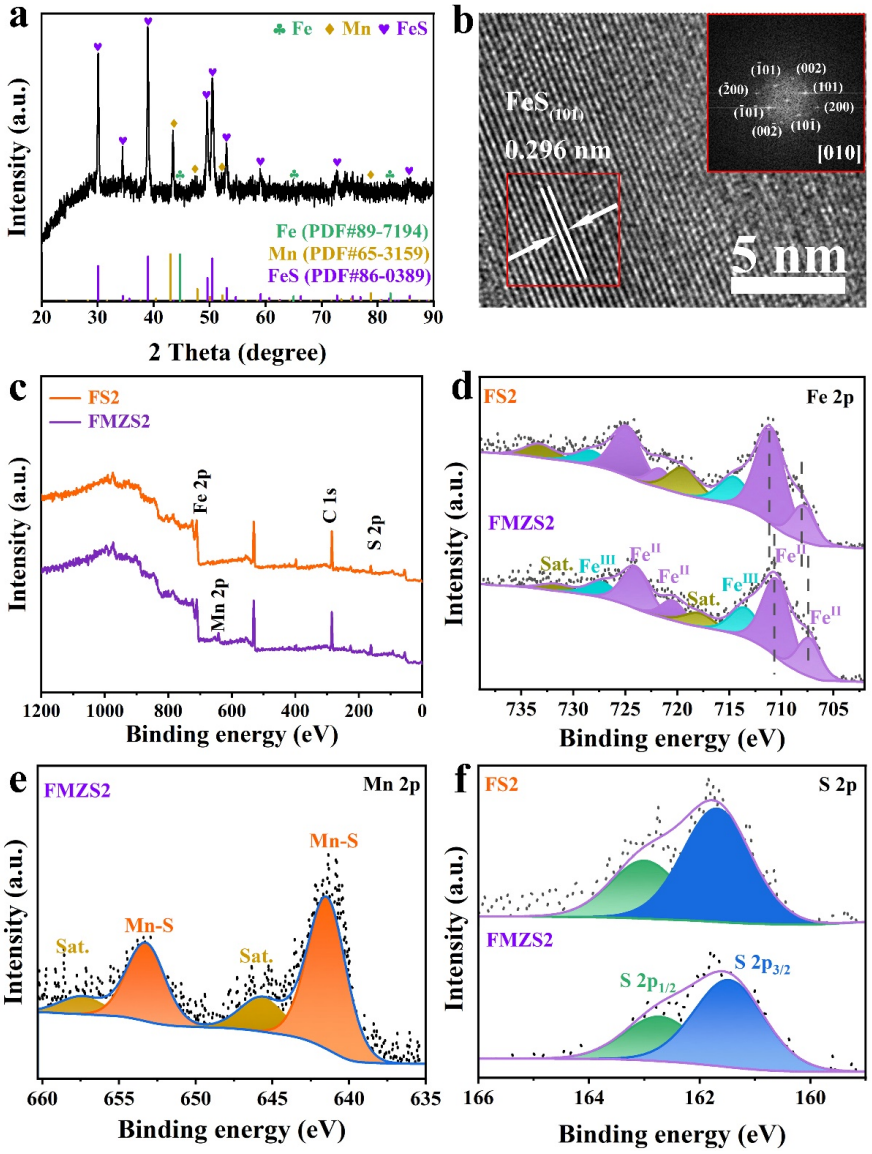

Figure 2. (a) XRD pattern of FMZS2; (b) HRTEM image of FMZS2, Inset: FFT pattern of FMZS2; (c) XPS survey spectrum of FS2 and FMZS2; High–resolution spectra of (d) Fe 2p , (e) Mn 2p and (f) S 2p for FS2 and FMZS2.

tetragonal FeS (PDF#86–0389). In addition the rest diffraction peaks are attributed to cubic Fe (PDF#89–7194) and cubic Mn (PDF#65–3159) in the skeleton. It is worth noting that Mn doping in the FeS does not induce obvious shift of the diffraction peaks due to the indistinguishable contrast between Fe and Mn atoms. The high–resolution transmission electron microscopy (HRTEM) image in **Figure 2b**shows obvious lattice fringes with an interplanar spacing of 0.296 nm, in agreement with the (101) planes of FeS, verified by the corresponding fast Fourier transform (FFT) pattern (inset of **Figure 2b**). The selective area electron diffraction (SAED) pattern at low magnification shows typical polycrystalline ring patterns with (001), (101), (110), (111), (112), (211) and (311) crystal planes (**Figure S4**), which is also consistent with XRD results. The X–ray photoelectron spectroscopy (XPS) analysis is performed to examine the surface chemical state and composition of FMZS2 with bare FS2 as a reference. Survey spectrum in **Figure 2c** shows the coexistence

Posted on 8 Feb 2023 — The copyright holder is the author/funder. All rights reserved. No reuse without permission. — https://doi.org/10.22541/au.167584896.64632955/v1 — This a preprint and has not been peer reviewed. Data may be preliminary.

of Fe, Mn and S elements of FMZS2. In **Figure 2d** , the high resolution Fe $2p$ XPS spectrum of FMZS2 shows that the 707.34 e V/720.43e V and 710.44/723.98 e V are indexed to the Fe $2p_{3/2}/2p_{1/2}$ of Fe species in Fe^{II}–S, in which the peaks with smaller binding energy actually represent the electron–deficient Fe^{II}sites caused by Fe–S bonds breaking in FeS compounds.[30] Most importantly, the Fe^{II}–S $2p_{2/3}$ peaks have partial negative shift from those of the Fe^{II}–S in FS2 (707.88 and 711.03e V).[31-33]The obvious charge redistribution comes from Mn doping in FeS compound, which may adjust the electronic structure of bare FeS. The other signals positioned at 713.42/727.22e V and 717.94/731.74 e V are corresponding to Fe $2p_{3/2}/2p_{1/2}$ of Fe^{III} states and their satellite structures from surface oxidation.[31-33] In the Mn $2p$spectrum (**Figure 2e**), the peaks positioned at 641.45/653.25e V and 645.70/657.50 e V are attributed to Mn $2p_{3/2}/2p_{1/2}$ in Mn^{II}–S and their satellite structures, respectively.[34] **Figure S5** shows the high–resolution spectrum of element Zn indicates its low content on the surface of FMZS2, which confirms Zn content does not interfere Mn–doped FeS phase. In the S $2p$ XPS spectrum (**Figure 2f**), the FMZS2 peaks of S $2p$positioned at 161.47/162.73 e V correspond to $2p_{3/2}/2p_{1/2}$ of S species, which represents metal sulfide (M–S).[32, 33] The microstructure characterization and chemical feature convincingly demonstrate that Mn–doped FeS nano–sheet vertically grown on FeMnZn skeleton (FeMnZn/Mn-FeS) hybrid electrode is successfully prepared.

The SEM measurements are also carried out on contrastive FS2, FZS2 and FMS2 in order to investigate the role of each element. In terms of the absence of Mn element, FZS2 exhibits hierarchical nano/micro sheet–to–sheet morphology without porous channel (**Figure S6a**). Accordingly, that open porous and ligament structure is stemmed from etching Mn can elevate mass transport and electron transfer as well as the vulcanizing degree of FMS2, verified by their XRD patterns (**Figure S7**). While, surprisingly, for the absence of Zn element, FMS2 only exhibits single–level nano–sheets with smooth surfaces (**Figure S6b**), originated from the lamellar morphology of metallic sulfide. For the hierarchical nano/micro sheet–to–sheet structure, micro–sheet has root in etching Zn atoms, and its vertical–grown sheet morphology also provide large surface area and abundant nucleation site for generating metallic sulfide nano–sheets. Furthermore, in the absence of both Mn and Zn elements, FS2 exhibits neither porous channel nor hierarchical nano/micro sheet–to–sheet morphology (**Figure S6c**), which also brings poor level of surface vulcanization and homogeneous FeS phase (**Figure S7**). Therefore, we can deduce that etching Mn atoms is in favor of forming porous structure while etching Zn atoms benefits forming micro–sheet morphology. Contact angles in air and water are important target that estimates the physical feature towards water splitting. For electrocatalyst contact with electrolyte, the surface should provide an interface that facilitates contact with the electrolyte to continuously provide sufficient reaction space to the catalytic active site. And for the bubble release process, the adhesion of bubbles on the surface of electrocatalyst should be reduced to facilitate the bubble release behavior. Therefore, contact angle of electrocatalysts in water and air are both measured. From **Figure S8** it can be found that the contact angle of FMZS2 in air (0^o) is significantly smaller than that of the other specimens, while in water (150^o) it is larger than that of the other specimens, which indicates that the surface of FMZS2 is super hydrophilic and super aerophilic. The open porous and hierarchical nano/micro sheet–to–sheet structure can significantly enhance the affinity for water droplets and the aversion to air.

2.2. Electrochemical analysis

Posted on 8 Feb 2023 — The copyright holder is the author/funder. All rights reserved. No reuse without permission. — https://doi.org/10.22541/au.167584896.64632955/v1 — This a preprint and has not been peer reviewed. Data may be preliminary.

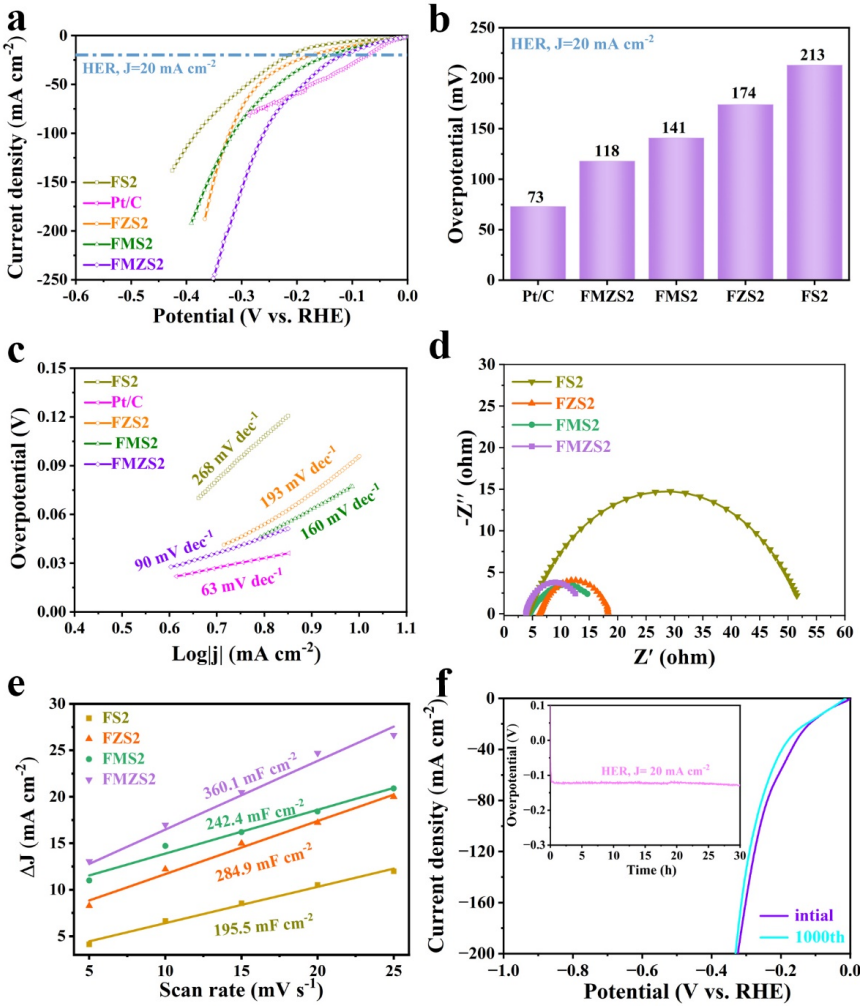

Figure 3. (a) LSV curves, (b) Overpotentials at 20 mA cm^{-2} and (c) Tafel slopes of electrocatalysts for HER in 1 M KOH electrolyte, respectively; (d) EIS spectra and (e) capacitive current versus scan rate of electrocatalysts; (f) Comparison of the initial and 1000th LSV curves of FMZS2, inset: chrono–potentiometric curves of FMZS2 at 20 mA $cm^{-2}$for HER.

The electrocatalytic activity of FMZS2 for HER in alkaline electrolyte is first evaluated in a representative three–electrode electrochemical configuration (**Figure 3a**). As a comparison, the HER catalytic activity of FS2, FZS2, FMS2 and commercial Pt/C are investigated. The FMZS2 exhibits the nearly lowest overpotential at the same current density than that of the other integrated sulfide electrocatalyst. Among them, FMZS2 only requires an overpotential of 118 mV to achieve 20 mA cm^{-2}, comparable with Pt/C (73 mV), while FMS2, FZS2 and FS2 require overpotentials of 141 mV, 174 mV and 213 mV, respectively (**Figure 3b**). Quite frankly, the excellent HER performance endows FMZS2 to be one of the top transition metal–based compounds among many published electrocatalysts (**Table S1**). Furthermore, FMZS2 surpasses commercial Pt/C under the high overpotential (> 213 mV), which is a rare quality required for industrial water electrolysis. The Tafel slope is an important indicator of the reaction kinetics and rate–determining steps, revealing the relationship between 10–fold current density and overpotential. For details of the HER procedure in alkaline electrolyte, see **Note S1** . The Tafel slope of FMZS2 is approximately 90 mV dec^{-1}, demonstrating the rapid Volmer–Heyrovsky mechanism and lower energy consumption in the

Posted on 8 Feb 2023 — The copyright holder is the author/funder. All rights reserved. No reuse without permission. — https://doi.org/10.22541/au.167584896.64632955/v1 — This a preprint and has not been peer reviewed. Data may be preliminary.

electrochemical processes. The electrochemical impedance spectroscopy (EIS) analysis further reveals the high–resolution reaction kinetics on the electrocatalyst surface. From the Nyquist plot (**Figure 3d**), it can be seen that the EIS spectrum of FMZS2 shows a small semicircle with low intrinsic resistance (R_s) and charge transfer resistance (R_{CT}). Fitting by equivalent circuit, the R_s and R_{CT} value of FMZS2 are determined to be ˜3.8 Ω and ˜8.7 Ω, respectively, which are much lower than the values of FMS2 (˜4.5 Ω and ˜10.2 Ω), FZS2 (˜6.2 Ω and ˜12.1 Ω) and FS2 (˜4.4 Ω and ˜47.2 Ω) electrodes (**Figure S9**). The smallest R_s and R_{CT} values of FMZS2 indicate that its open porous–structure and self–supported electrode promote the conductivity and interfacial charge transfer efficiency. Further, the electrochemical surface area (ECSA) is evaluated by doule–layer capacitance (C_{dl}), which is assessed by cyclic voltammetry (CV) curves in the non–Faraday range at different scan rates (0.074–0.174 V, 5–25 mV s^{-1}, **Figure S10**). The C_{dl} of FMZS2 is 360.1 mF cm^{-2}, significantly higher than those of FMS2 (242.4 mF cm^{-2}), FZS2 (284.9 mF cm^{-2}) and FS2 (195.5 mF cm^{-2}, **Figure 3e**). Such large active surface area of FMZS2 profits from its porous and hierarchical–vertical–sheet morphology. Moreover, the intrinsic activities of these electrodes are estimated by normalization of the linear sweep voltammetry (LSV) curve of HER by ECSA (**Figure S11**). The LSV curves of FMZS2 and FMS2 are basically in coincidence, similar to FZS2 and FS2, which further confirms Zn elements favor to generate the advantageous morphology with hierarchical sheet–to–sheet and have no effect on the improvement of intrinsic activity. In addition, at overpotential of 250 mV, the intrinsic activity of FMZS2 is 0.23 mA $cm^{-2}{}_{ECSA}$, which is 1.43 fold greater than that of FS2 (0.16 mA $cm^{-2}{}_{ECSA}$), which suggests that the doping of Mn in FeS endow such an enhancement on HER intrinsic activity. As shown in **Figure S12** , it is also verified by the higher turnover frequency (TOF) of FMZS2 than that of FS2. At overpotential of 200 mV, the TOF of FMZS2 (0.013 s^{-1}) is 1.78 times higher than that of FS2 (0.0073 s^{-1}). Besides its remarkable catalytic activity, long–term durability is a crucial feature in the practical application of electrocatalysts. As can be seen from **Figure 3f** , the LSV curve of FMZS2 after 1000 cycles is almost consistent with the initial one, indicating that FMZS2 has significant cycling stability. Meanwhile, the FMZS2 is also confirmed to be super stable by the overpotential–time curve in inset of **Figure 3f** . The overpotential increases slightly compared to the initial one at 20 mA cm^{-2} after 30 h. These results indicate that FMZS2 is a stable HER electrocatalyst under alkaline condition, which should be attributed to the robust and self–supported electrode skeleton. The morphology and surface chemical state of electrocatalysts after durability tests are probed by SEM and XPS. The SEM images (**Figure S13a and b**) show that the sheet and porous skeleton structure is still maintained. Also, the high–resolution XPS spectra confirm that the main elements in Mn–FeS basically maintain the initial chemical states (**Figure S14, S15**). However, the absence of electron–deficient Fe^{2+} sites in Fe–S bonds and decrease of S content are presumed to the OH* coverage during the electrolysis under alkaline environment, according to the EDS (**Figure S13c**) and XPS (**Figure S14**) spectra.

Posted on 8 Feb 2023 — The copyright holder is the author/funder. All rights reserved. No reuse without permission. — https://doi.org/10.22541/au.167584896.64632955/v1 — This a preprint and has not been peer reviewed. Data may be preliminary.

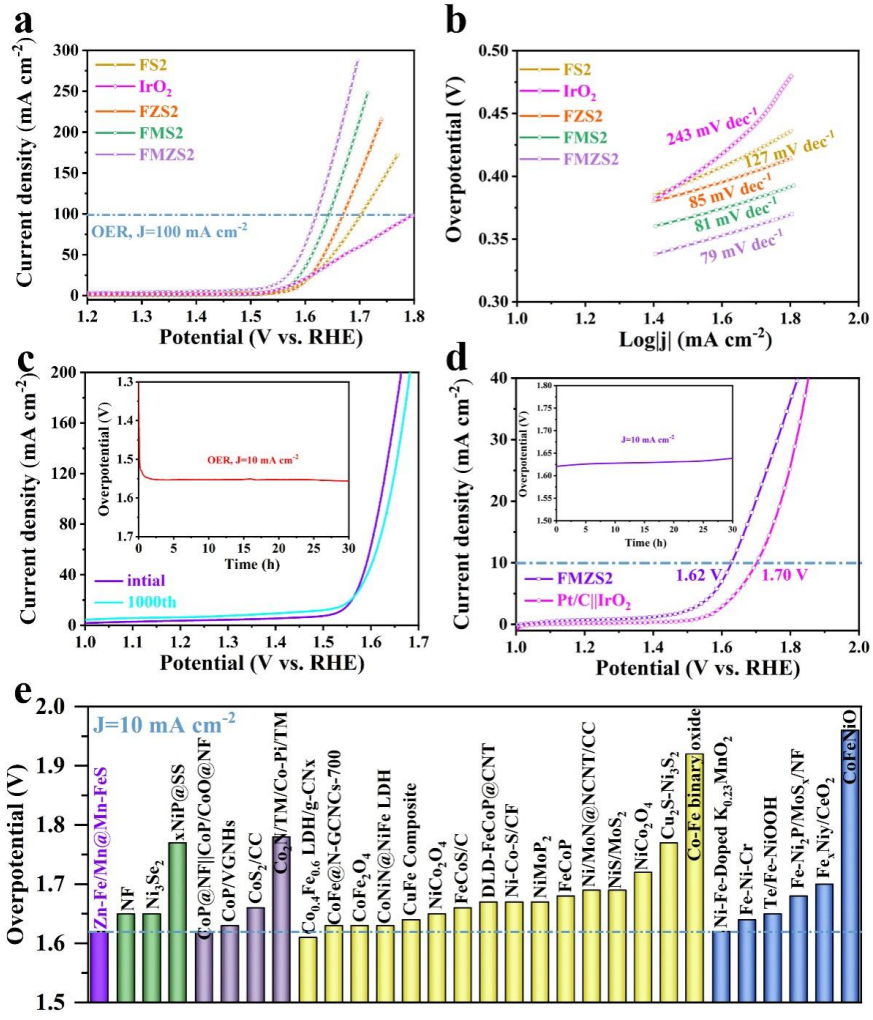

Figure 4. (a) LSV curves, (b) Tafel slopes of electrocatalysts for OER in the equivalent electrolyte, respectively; (c) Comparison of the initial and 1000th LSV curves of FMZS2, Inset: chrono–potentiometric curves of FMZS2 at 10 mA $cm^{-2}$for OER; (d) LSV curves of FMZS2 and Pt/C||IrO_2 for overall water splitting, Inset: chrono–potentiometric curve of FMZS2; (e) Comparison of FMZS2 overpotential at 10 mA cm^{-2} with previously reported counterparts.

Furthermore, the electrochemical OER activity of these electrocatalysts in the identical electrolyte is also determined. As shown in**Figure 4a** , the LSV curves of electrocatalysts are displayed and the electrocatalytic activities of different electrodes follow the trend of IrO_2 <FS2 < FZS2 <FMS2 <FMZS2. The overpotentials required to reach 100 mA cm^{-2} are 390 mV, 413 mV, 440 mV, 470 mV and 578 mV for FMZS2, FMS2, FZS2, FS2, and IrO_2, respectively. The performance of FMZS2 remains outstanding compared to previously reported catalysts with the identical functionality, for instance, Ni_2Mo_3N/NF (392 mV),[35]$MoSe_2$–Ni_3Se_2/NF (395 mV),[36]CuCo–Ni_3S_2/NF (400 mV)[37] and FeNi/NF (420 mV),[38]etc. (**Table S2**) Subsequently,**Figure S16** further illustrates the OER intrinsic activity, in which the LSV curve is normalized by ECSA. The intrinsic activity of FMZS2 is 0.79 mA $cm^{-2}{}_{ECSA}$ at 450 mV, ˜2.02–fold greater than that of FS2 (0.39 mA $cm^{-2}{}_{ECSA}$). In view of these discussions, the enhanced HER and OER intrinsic activity and electroactive surface area is probably due to the doping of heterogeneous Mn atoms in FeS and the typical porous, hierarchical nano/micro sheet–to–sheet structure. The corresponding OER electrocatalytic kinetics

Posted on 8 Feb 2023 — The copyright holder is the author/funder. All rights reserved. No reuse without permission. — https://doi.org/10.22541/au.167584896.64632955/v1 — This a preprint and has not been peer reviewed. Data may be preliminary.

are shown in **Figure 4b** . The Tafel slopes of 79 mV dec^{-1}, 81 mV dec^{-1}, 85 mV dec^{-1}, 127 mV dec^{-1} and 243 mV dec^{-1} for FMZS2, FMS2, FZS2, FS2 and IrO_2, respectively, indicating that the FMSZ2 has the fastest reaction rate as well as the lowest energy consumption. For specific OER reaction steps, see **Note S1** .

The cycle stability and long–term durability of FMZS2 are also tested.**Figure 4c** shows the overpotential–time curve of FMZS2 at 10 mA cm^{-2} for 30 h. As shown in inset of **Figure 4c** , the LSV curve after 1000 CV cycles has slightly shift compared to the initial curve. Surprisingly, negligible changes and slight overpotential decay can be observed. The specimens are characterized by SEM, XPS and EDS after testing the durability of OER. The SEM images (**Figure S17a and b**) show that the morphological changes are not obvious, indicating the excellent structural stability of the electrocatalyst. The EDS spectra (**Figure S17c**) and XPS survey spectra (**Figure S18**) can be seen that there is no significant change except for element S. It can be seen by XPS that metal elements remain their original chemical valence (**Figure S19**). While the content of M–S element is slightly reduced and the surface S content decreases, verified by EDS and XPS, which indicates in–situ formation of an oxide layer on the surface of FMZS2 under OER measurement.

The good electrocatalytic performance of FMZS2 for both HER and OER indicates their real potential for overall water splitting. The electrons are transferred from the anode to the cathode to provide electrical energy for production of H_2 at the cathode and O_2 at the anode during the electrolysis process. FMZS2 requires an overpotential of 1.62 V at 10 mA cm^{-2}, lower than that of Pt/C||IrO_2 (1.70 V) and reported electrocatalysts (**Figure 4d,e** and **Table S3**). Faradaic efficiency experiments are carried out on FMZS2 (cathode and anode) in a sealed H–type electrolyzer (**Figure S20a and b**). H_2 is collected in a cylinder with a blue liquid and O_2 is collected in a cylinder with a pink liquid at 30 mA cm^{-2} for 30 min. The volumes of $H_2$and O_2 produced are calculated by recording the curves of liquid level versus time, and finally the faradaic efficiency is obtained (**Figure S20c,d, TableS4** and **Note S3**). The volume ratio of H_2 to O_2 produced is in general agreement with the theoretical value (2:1), and the faradaic efficiency of the overall water splitting is also calculated to nearly 100% during the electrolysis. The durability measurement shows good activity retention at 10 mA cm^{-2} for 30 h (**inset of Figure 4d**), indicating that FMSZ2 has stable overall water splitting performance.

The DFT calculations is performed to obtain atomic–level insight of the enhanced intrinsic activity of FMZS2. For HER process, the Gibbs free energy of hydrogen adsorption (ΔG_{H^*}) is a valid descriptor that closer to zero meaning the optimal intrinsic activity of the electrocatalyst, because the adsorbed hydrogen atoms (*H) are in a thermoneutral state that is beneficial to balance proton/electron coupling and molecular hydrogen release. Two slab models of FS2 and FMZS2 (**Figure 5a)** are constructed for the evaluation of possible electroactive sites. The top_{Mn}, $top_{S1}$and top_{S2} sites of *H adsorption are considered on FS2 and FMZS2, labeled as FS2 top_{S1}, FS2 top_{S2}, FMZS2 top_{Mn}, FMZS2 top_{S1} and FMZS2 top_{S2} (**Figure S21** and **Figure 5b**). As shown in **Figure 5c** , the ΔG_{H^*} of FMZS2 top_{S1} is -0.029 eV lower than the others (FMZS2 top_{S2} (0.20 eV), FMZS2 top_{Mn} (0.78 eV), FS2 top_{S1} (-0.36 eV), FS2 top_{S2} (0.53 eV)). The lowest ΔG_{H^*} of FMZS2 top_{S1}indicates that the Mn doping trigger high catalytic FMZS2 top_{S1} sites, which is favorable adsorption/desorption of H* species and thus facilitate the HER kinetics. Meanwhile, the introduction of Mn species in FeS significantly increases the density of states (DOS) on the Fermi energy of the whole system relative to FeS has been demonstrated.[39] The high DOS of Mn-FeS indicates that more charge carriers can directly participate in the catalytic reaction, which contributes to a significant improvement of the catalytic performance.[40] In addition, the DOS intensity at the Fermi energy level is closely related to the conductivity. The increased DOS intensity of Mn-FeS indicates that a fast charge transfer kinetics, which is highly consistent with the charge transfer resistance in **Figure 3d** .

While for OER process, its energetics are related to the adsorption behaviour of oxygen–related intermediates (*O, *OH and *OOH) based on Sabatier's adsorbate evolution mechanism (**Note S1**). As shown in**Figure 5d** , stepwise plots of Gibbs free energies on FMZS2 top_{S1} and FS2 top_{S1} are calculated. The results show that the formation *OOH from *O (*O + OH^- - *OOH + e^-) is the step that determines the reaction rates

of FMZS2 and FS2. After the formation of the Mn–S bond in Mn–FeS, the energy barrier of FMZS2 top_{S1} is reduced to 1.447 eV, compared with that of FS2 top_{S1} (1.575 eV). DFT simulation indicates the S site adjacent to Mn in FMZS2 favors to overcome the energy barrier and thus accelerate the OER kinetics. The DFT results demonstrate that the composition modulation for FeS is viable to balance the adsorption and desorption of intermediate species during HER and OER process, which confer a remarkable electrocatalytic activity towards overall water splitting.

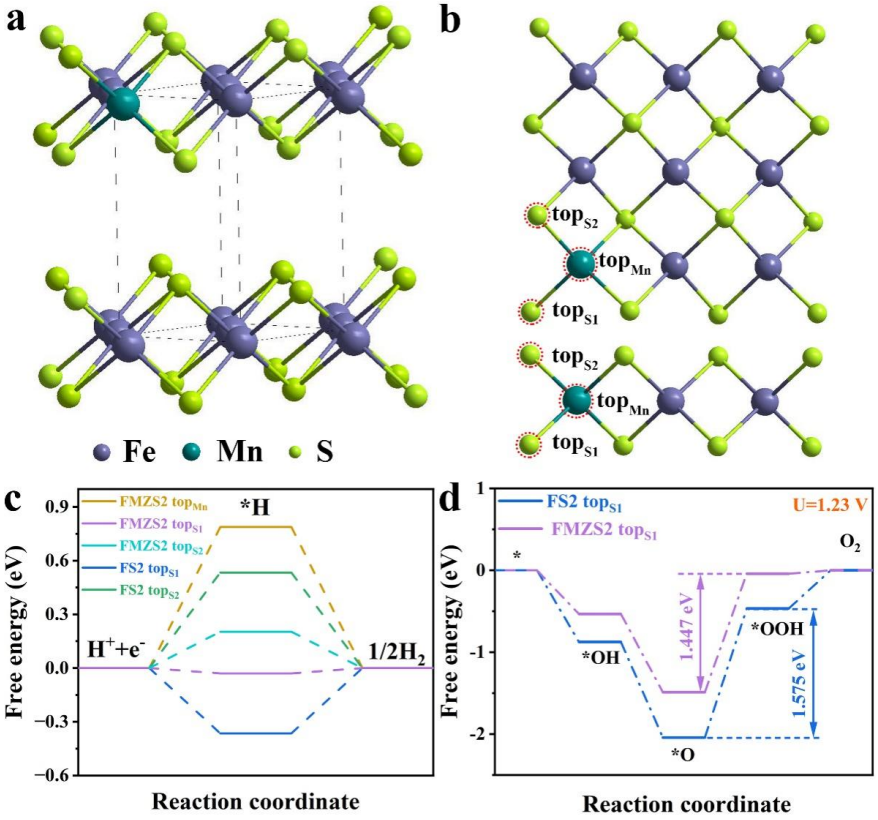

Figure 5. (a) Crystal structure schematic of Mn doped FeS. (b) Top view (top) and side view (below) slab model of FMZS2; (c) Calculated free–energy diagram of HER on possible adsorption sites, containing FS2 top_{S1}(blue), FS2 top_{S2}(green), FMZS2 top_{S1}(purple), FMZS2 top_{S2} (indigo) and FMZS2 top_{Mn} (brown); (d) The free–energy diagram of OER on FS2 top_{S1} and FMZS2 top_{S1} sites.

3. Conclusion

In summary, we present a FeMnZn/Mn-FeS electrocatalyst with hierarchical nano/micro sheet–to–sheet structure vertically wrapped on porous multi–metal skeleton by etching and subsequent sulfuration. By virtue of component optimization and morphology design, *i.e.* heterogeneous atom doping, hierarchical nano/micro sheet–to–sheet and porous structure stemmed from functional role of Mn and Zn elements, FMZS2 delivers the overpotential of 118 mV and 390 mV to achieve a 20 mA cm^{-2} and 100 mA cm^{-2} for HER and OER, respectively, which is the smallest ones among these integrated metal sulfide electrocatalyst. In terms of HER performance, FMZS2 even surpasses the commercial Pt/C under high current density. FMZS2 also has small Tafel slope and long durability performance as a bifunctional electrocatalyst. This simple and facile method can be widely used to prepare self–supported electrodes of bimetallic or polymetallic compound with morphological engineering for various electrochemical energy applications.

4. Experimental Section/Methods

Posted on 8 Feb 2023 — The copyright holder is the author/funder. All rights reserved. No reuse without permission. — https://doi.org/10.22541/au.167584896.64632955/v1 — This a preprint and has not been peer reviewed. Data may be preliminary.

Posted on 8 Feb 2023 — The copyright holder is the author/funder. All rights reserved. No reuse without permission. — https://doi.org/10.22541/au.167584896.64632955/v1 — This a preprint and has not been peer reviewed. Data may be preliminary.

4.1. Preparation of electrocatalysts : First, $Fe_{70}Mn_{28}Zn_2$ (wt%, FMZ1) with thickness of ˜300 μm was etched in a 3 wt% HCl solution for 1 h to obtain FeMnZn alloy (FMZ2). The FeMnZn/Mn-FeS (FMZS2) electrocatalyst was prepared via one–step hydrothermal method by adding FMZ2 to 20 mL thiourea solution (5 mg/mL), conditions: 160°C, 24 h. FS2, FZS2 and FMS2 were also produced by similar methods using Fe, $Fe_{93}Zn_7$ and $Fe_{72}Mn_{28}$ as precursors, respectively. The reference ink was prepared by adding 20 mg of noble metal electrocatalyst (20 wt% Pt/C or IrO_2) to 1 mL solution (49% deionized water, 49% ethanol and 2% Nafion) by sonication for 30 min. 5 μL inks were drop–cast onto glassy carbon electrode.

4.2. Characterization : The morphological and structure of the specimens were carried out by SEM measurement on JSM–6700F (JEOL) electron microscope equipped with EDS and TEM measurement on TF20 (JEOL) microscope, respectively. The XRD and XPS measurements of the specimens were performed on a Rigaku D/max–IIB X–ray diffractometer (monochromatic Cu K_α radiation) and on a Thermo ECSALAB 250Xi with an Al anode, respectively. Charging effects were compensated by shifting binding energies according to the C 1s peak (284.8e V). Contact angle testing of specimens was performed on a contact angle meter (KINO–Co, USA) and photographed with a camera (5D Mark IV, Canon, Japan).

4.3. Electrochemical measurements : Electrochemical measurements were carried out in a three–electrode configuration with specimens, graphite rod and Hg/HgO electrode as the working, counter and reference electrodes, respectively. All overpotentials were compensated with 90% iR and recorded relative to the reversible hydrogen electrode (RHE): $E_{RHE} = E_{Hg/HgO} + 0.059pH + 0.098$ V. The polarization curves were collected in alkaline electrolyte with the scan rate of 5 mV s^{-1}. EIS measurements were conducted at overpotential of 250 mV with frequency ranging from 10^5 to 10^{-2} Hz. CV curves of the specimens were accumulated under various scan rates in order to determine their double layer capacitance (C_{dl}) values and used to evaluate ECSA. Long–term overpotential *vs.* time tests of FMZS2 were carried out at 20 mA cm^{-2} (HER) and 10 mA cm^{-2} (OER) for 30 h, respectively. The Faradaic efficiency is evaluated by water drainage method, which FMZS2 carried out overall water splitting at 30 mA cm^{-2} for 30 min and the produced H_2 and O_2volumes are recorded at every five minutes.

4.4. Theoretical Calculation : DFT-based first-principles calculations were carried out with the Vienna Ab-initio Simulation Package (VASP) implemented using the Perfew–Burke–Ernzerhof exchange–correlation potential and the projector augmented plane-wave (PAW) method.[41-44] Convergence tests for the number of K points and the plane wave cut-off energies were performed, leading to the present setting of a plane wave cutoff energy of 400 eV, and the k-point mesh of 4×4×1. These settings assure converge criteria for the energy and force were 1×10^{-4} eV and 0.05 eV $Å^{-1}$, respectively. The slabs of six layers (2×1) of FeS (101) and Mn–FeS (101) surfaces, with the bottom three layers fixed during the optimization, were created. The computational hydrogen electrode model was used to study the HER and the OER,[45] and the Gibbs free energy was calculated by considering the zero–point energy and entropy of adsorbates.[46]

Acknowledgements

L. Huang and R. Yao contributed equally to this work. This work was supported by the National Natural Science Foundation of China (grant Nos. 51601067, 22071020, 22271043, 22205034), Science and Technology Development Program of Jilin Province (grant Nos. 20160520007JH, 20220101045JC), the Fundamental Research Funds for the Central Universities (grant Nos. 2412021QD008, 2412022QD012) and the Program for JLU Science and Technology Innovative Research Team (JLUSTIRT, 2017TD–09). The author would like to thank shiyanjia lab (www.shiyanjia.com) for the support of the preparation process schematic.

Conflict of Interest

There are no conflicts to declare.

Supporting Information

Supporting Information is available from the Wiley Online Library or from the author.

Keywords

Posted on 8 Feb 2023 — The copyright holder is the author/funder. All rights reserved. No reuse without permission. — https://doi.org/10.22541/au.167584896.64632955/v1 — This a preprint and has not been peer reviewed. Data may be preliminary.

hierarchical nano/micro sheet-to-sheet, heterogeneous doping sulfide, integrated structure, electrocatalyst, overall water splitting

References

[1] S. Chu, A. Majumdar, Nature **2012,** 488, 294-303.

[2] J. A. Turner, Science **2004,** 305, 972-974.

[3] M. G. Walter, E. L. Warren, J. R. McKone, S. W. Boettcher, Q. Mi, E. A. Santori, N. S. Lewis, Chem. Rev. **2010,** 110, 6446-6473.

[4] V. R. Stamenkovic, D. Strmcnik, P. P. Lopes, N. M. Markovic, Nat. Mater. **2017,** 16, 57-69.

[5] I. Roger, M. A. Shipman, M. D. Symes, Nat. Rev. Chem.**2017,** 1, 1245-1251.

[6] J. Mahmood, F. Li, S.-M. Jung, M. S. Okyay, I. Ahmad, S.-J. Kim, N. Park, H. Y. Jeong, J.-B. Baek, Nature Nanotechnology **2017,**12, 441-446.

[7] N. Mahmood, Y. Yao, J.-W. Zhang, L. Pan, X. Zhang, J.-J. Zou, Adv. Sci. **2018,** 5, 1700464.

[8] W. Sheng, M. Myint, J. G. Chen, Y. Yan, Energy Environ. Sci.**2013,** 6, 1509-1512.

[9] X. Zou, Y. Zhang, Chemical Society Reviews **2015,** 44, 5148-5180.

[10] J. K. Norskov, C. H. Christensen, Science **2006,** 312, 1322-1323.

[11] W.-J. Jiang, S. Niu, T. Tang, Q.-H. Zhang, X.-Z. Liu, Y. Zhang, Y.-Y. Chen, J.-H. Li, L. Gu, L.-J. Wan, J.-S. Hu, Angew Chem Int Edit**2017,** 56, 6572-6577.

[12] B. Seo, G. Y. Jung, Y. J. Sa, H. Y. Jeong, J. Y. Cheon, J. H. Lee, H. Y. Kim, J. C. Kim, H. S. Shin, S. K. Kwak, S. H. Joo, Acs Nano**2015,** 9, 3728-3739.

[13] L. Huang, Y. Yang, C. Zhang, H. Yu, T. Wang, X. Dong, D. Li, Z. Liu, Nanotechnology **2020,** 31, 225403.

[14] L. Huang, L. Xu, Y. Yang, H. Yu, H. Tao, D. Li, X. Dong, J Mater Sci-mater El **2020,** 31, 6607-6617.

[15] Z. X. Jing, Q. Y. Zhao, D. H. Zheng, L. Sun, J. H. Geng, Q. N. Zhou, J. J. Lin, J. Mater. Chem. A **2020,** 8, 20323-20330.

[16] S. Enthaler, K. Junge, M. Beller, Angew Chem Int Edit**2008,** 47, 3317-3321.

[17] X. Zou, Y. Wu, Y. Liu, D. Liu, W. Li, L. Gu, H. Liu, P. Wang, L. Sun, Y. Zhang, Chem **2018,** 4, 1139-1152.

[18] J. Zhang, Y. Wu, H. Hao, Y. Zhang, X. Chen, K. Xing, J. Xu, Electrochim. Acta **2022,** 402, 139554.

[19] M. Villalba, J. Peron, M. Giraud, C. Tard, Electrochem. Commun.**2018,** 91, 10-14.

[20] S. N. A. Zakaria, N. Hollingsworth, H. U. Islam, A. Roffey, D. Santos-Carballal, A. Roldan, W. Bras, G. Sankar, G. Hogarth, K. B. Holt, N. H. de Leeuw, ACS Appl. Mater. Interfaces **2018,** 10, 32078-32085.

[21] Z. Jing, Q. Zhao, D. Zheng, L. Sun, J. Geng, Q. Zhou, J. Lin, J. Mater. Chem. A **2020,** 8, 20323-20330.

[22] G. Zhang, Y.-S. Feng, W.-T. Lu, D. He, C.-Y. Wang, Y.-K. Li, X.-Y. Wang, F.-F. Cao, ACS Catal. **2018,** 8, 5431.

[23] Y. Pan, Y. Liu, Y. Lin, C. Liu, ACS Appl. Mater. Interfaces**2016,** 8, 13890-13901.

[24] X. Xu, Y. Ge, M. Wang, Z. Zhang, P. Dong, R. Baines, M. Ye, J. Shen, ACS Appl. Mater. Interfaces **2016,** 8, 18036-18042.

Posted on 8 Feb 2023 — The copyright holder is the author/funder. All rights reserved. No reuse without permission. — https://doi.org/10.22541/au.167584896.64632955/v1 — This a preprint and has not been peer reviewed. Data may be preliminary.

[25] D. Zheng, Z. Jing, Q. Zhao, Y. Kim, P. Li, H. Xu, Z. Li, J. Lin, Chemical Engineering Journal **2020,** 402, 125069.

[26] L. Wang, Y. Shan, L. Liu, Mater. Chem. Phys. **2020,**239, 122046.

[27] B. T. Yonemoto, G. S. Hutchings, F. Jiao, Journal of the American Chemical Society **2014,** 136, 8895-8898.

[28] S. Niu, W. J. Jiang, T. Tang, L. P. Yuan, H. Luo, J. S. Hu, Adv. Funct. Mater. **2019,** 29, 1902180.

[29] Z. Pan, M. Yaseen, P. Kang Shen, Y. Zhan, J. Colloid Interface Sci. **2022,** 616, 422-432.

[30] I. Uhlig, R. Szargan, H. W. Nesbitt, K. Laajalehto, Applied Surface Science **2001,** 179, 222-229.

[31] I. Uhlig, R. Szargan, H. W. Nesbitt, K. Laajalehto, Applied Surface Science **2001,** 179, 222-229.

[32] T. X. Nguyen, Y.-H. Su, C.-C. Lin, J.-M. Ting, Advanced Functional Materials **2021,** 31, 06229.

[33] R. Miao, B. Dutta, S. Sahoo, J. He, W. Zhong, S. A. Cetegen, T. Jiang, S. P. Alpay, S. L. Suib, Journal of the American Chemical Society**2017,** 139, 13604-13607.

[34] M. C. Biesinger, B. P. Payne, A. P. Grosvenor, L. W. M. Lau, A. R. Gerson, R. S. C. Smart, Applied Surface Science **2011,** 257, 2717-2730.

[35] S. H. Park, S. H. Kang, D. H. Youn, Materials **2021,**14, 4768.

[36] Y. Liu, Y. Liu, Y. Yu, C. Liu, S. Xing, Frontiers in Energy**2022,** 16, 483–491.

[37] J.-F. Qin, M. Yang, S. Hou, B. Dong, T.-S. Chen, X. Ma, J.-Y. Xie, Y.-N. Zhou, J. Nan, Y.-M. Chai, Appl. Surf. Sci. **2020,**502, 144172.

[38] T. E. Seuferling, T. R. Larson, J. M. Barforoush, K. C. Leonard, ACS Sustainable Chem. Eng. **2021,** 9, 16678-16686.

[39] H. Chen, X. Yang, P. Lv, P. Tian, S. Wan, Q. Liu, Chemical Engineering Journal **2022,** 450, 137960.

[40] B. Qiu, L. Cai, Y. Wang, Z. Lin, Y. Zuo, M. Wang, Y. Chai, Advanced Functional Materials **2018,** 28, 1706008.

[41] G. Kresse, D. Joubert, Physical Review B **1999,** 59, 1758-1775.

[42] P. E. Blöchl, Physical Review B **1994,** 50, 17953-17979.

[43] G. Kresse, J. Furthmüller, Physical Review B **1996,** 54, 11169-11186.

[44] J. P. Perdew, K. Burke, M. Ernzerhof, Physical Review Letters**1996,** 77, 3865-3868.

[45] J. K. Nørskov, J. Rossmeisl, A. Logadottir, L. Lindqvist, J. R. Kitchin, T. Bligaard, H. Jónsson, The Journal of Physical Chemistry B**2004,** 108, 17886-17892.

[46] M. Kunitski, N. Eicke, P. Huber, J. Köhler, S. Zeller, J. Voigtsberger, N. Schlott, K. Henrichs, H. Sann, F. Trinter, L. P. H. Schmidt, A. Kalinin, M. S. Schöffler, T. Jahnke, M. Lein, R. Dörner, Nature Communications **2019,** 10, 1.